

A modified energy-based fatigue parameter for short fibre reinforced polymers: performance analysis with varying thicknesses, load ratios and fibre orientations

F. E. Fiorini ^{1,2*}, L. M. Martulli ², P. Steck ¹, A. Bernasconi ²

¹ thyssenkrupp Presta AG, Competence Center Mechanics, Principality of Liechtenstein

² Politecnico di Milano, Mechanical Engineering Department, Via La Masa 1, 20156
Milano, Italy

*Corresponding author: francesco.fiorini@thyssenkrupp-automotive.com

Abstract

The durability of Short Fibre Reinforced Polymers (SFRPs) is affected by several variables. Accurate unifying fatigue parameters are thus essential for an efficient characterization campaign. This research investigated the fatigue behaviour of a Polyphthalamide PA6T/6I reinforced with 50% of glass fibres. Two thicknesses (1.6 mm and 3 mm), two orientations from the injection moulding direction (0° and 90°) and three load ratios (-0.5, 0.1, 0.5) were investigated. A new fatigue parameter, called Alternating Energy Density (AED), was presented; its ability to correlate the fatigue tests results was compared to other known fatigue parameters – cyclic mean strain rate and cyclic creep energy density. All the fatigue parameters were found to be independent of specimen thickness. Furthermore, the prediction of the fatigue lifetime based on AED showed greater accuracy with respect to the other known investigated methods. AED could thus be used for accurate and efficient lifetime prediction of SFRPs.

Keywords: short fibre-reinforced thermoplastic; fatigue parameter; anisotropy; load ratio; thickness.

1 Introduction

Increasingly restrictive regulations concerning global warming and greenhouse emissions have forced car manufacturers to prioritize the development of fuel-efficient and lightweight vehicles. Lightweight design and wide application of reinforced plastic materials, such as Short Fibres Reinforced Polymers (SFRPs), are thus becoming of primary importance. In the design of automotive components, the use of SFRPs can offer

several benefits. Their high strength-to-weight ratio can help reduce the overall weight of vehicle components, leading to an improved overall efficiency. They provide design flexibility, where moulding SFRPs into complex shapes allows more freedom in the design of automotive components. Furthermore, SFRPs can provide a cost-effective solution for automotive components as they can be manufactured using low-cost moulding processes.

Accurately predicting the fatigue behaviour of SFRPs is essential for their successful adoption into automotive components. Predicting the fatigue behaviour of SFRPs can be challenging due to several variables, including the material behaviour (type of the fibres, orientation of the fibres¹⁻⁴, matrix material, fibre-matrix interface), the inhomogeneous and anisotropic nature of the material structure (heterogeneous orientation and the three layer structure¹⁻⁶), loading conditions (mean stress⁷⁻¹⁰, strain rate^{11,12}, loading frequency¹¹), influence of environmental effects such as temperature and humidity¹³.

Due to all the listed variables, the orientation of the fibres plays an important role. It determines the degree of anisotropy and has a crucial influence on the stress state or triaxiality and its distribution within the component. In the thickness of the specimen, the fibre orientation varies. This microstructure has been widely discussed in the literature and is commonly known as a skin-shell-core microstructure^{1,2,5}. Due to the thermal shock, the skin layer is between the injected material and the mould walls. The fibres are frozen in their position and orientation, leading to randomly oriented fibres. The shell layer is the largest layer, where the shear stress of the material flow orientates the fibres in the injection moulding direction. The core layer is located in the centre part of the specimen. Contrary to the shell layer, here the fibres are perpendicular to the injection moulding direction. This fibre orientation is due to an extensional flow during the injection moulding process⁵.

As listed previously, the environmental effects and loading conditions are variables that must also be considered in the fatigue failure assessment. For example, the effect of the mean stress on the fatigue response of SFRPs was studied by Mallick and Zhou⁷. They performed tension – tension fatigue tests at different stress ratios. A significant effect on the SN diagram was observed. The fatigue strength decreased with increasing mean stress ratio. Additionally, the mean strain during the fatigue increased, which was attributed to

the creep caused by constant mean stress applied during the fatigue cycles. It is concluded that the stress amplitude-mean could be fitted by a parabolic relationship. The equation, called modified Gerber equation appears to represent the mean stress effects well.

The influence of the loading frequency to the fatigue strength was studied by Bernasconi and Kulin ¹¹. Tensile-tensile fatigue tests at a frequency ranging from 1 Hz to 4 Hz were performed. The authors concluded that an increase in frequency is related to a decrease in fatigue strength.

All these variables together increase the complexity in predicting the fatigue response of SFRP materials and components. Moreover, achieving a comprehensive characterization of an SFRP necessitates a substantial number of tests involving variations in parameters such as fibre orientation, testing temperature, load ratio, specimen thickness, among others. Therefore, it becomes crucial to identify a fatigue parameter capable of correlating the experimental fatigue data. Such a parameter can be experimentally determined for a specific testing configuration. Together with a constitutive model describing the cyclic behaviour implemented in a finite element tool, an accurate lifetime prediction for a component could be performed. This approach would significantly reduce the number of fatigue tests required for a complete characterization, thereby minimizing associated costs and time requirements. To predict the fatigue response of SFRP and identify such correlating parameter, several approaches are available in the literature. These approaches can be classified in various categories. The first category comprises the stress-based approaches where the stress components are the inputs. The failure parameter is determined by normalising the operating stress by the ultimate tensile stress results obtained from quasi-static uniaxial tensile tests ^{1,6}. This improved parameter has been found to give good results in predicting material failure under cyclic loading. Additionally, using this parameter does not require extensive experimental testing of the material under cyclic loading conditions, which can be time-consuming and expensive. The limitation of stress-based approaches is that a single set of parameters cannot fully describe the influence of the load ratio. To address this limitation, the model needs to include additional parameters and functions that can capture the material's behaviour under various load ratios, effects of ratcheting and cyclic creep failure ^{7,12}.

Part of the second category of failure prediction are parameters based on strain and parameters based on the energy. The cyclic quantities used for the failure prediction are typically calculated during cyclic loading in the stationary state^{14,15}. The evolution of these quantities such as secant modulus, cyclic energy density, hysteresis energy density, and dissipated energy density are stabilized. The fatigue prediction parameters such as cyclic creep increment³, elastic strain energy^{16,17} and dissipated energy¹⁸⁻²¹, are typically based on one of the mentioned cyclic quantities. The fatigue prediction, based on the mentioned parameters, is quite good and it was found that the data was independent of the orientation and environmental conditions. A limitation for the mentioned parameters is their ability to describe negative and positive load ratios. This limitation is in the nature of the mentioned parameters. For example, a fatigue failure prediction parameter based on the creep increment will not be able to describe negative load ratios (no creep occurs), while parameters based on the cyclic loop will fail to describe high load ratios.

Raphael et al.²² proposed the strategy for mixed fatigue prediction parameters. The approach was to combine the hysteresis energy density and the cyclic mean strain rate. The hysteresis energy density was able to unify results for the negative load ratios, and on the other hand the cyclic mean strain rate for positive load ratios. To optimize the transition between negative and positive load ratios, Raphael et al.²² introduced a second variant of the previous fatigue failure parameter where a weight function was used. This enabled a smooth transition between the areas governed by the cyclic mean strain rate and the hysteresis energy density. An increase in accuracy (scatter band 3) in fatigue failure prediction from 84% to 92% could be established.

Santharam et al.¹³, after an intensive study of different fatigue failure parameters applied the strategy to combine two fatigue failure parameters. They proposed two energy-based mixed parameters. The first fatigue failure parameter combines the creep energy density and the hysteresis energy density. The second variant combines the creep energy density and the cyclic energy density. The advantage of the second variant was that the cyclic energy density, compared to the hysteresis energy density, requires simpler mechanical models for the calculation. This approach enables an improvement in the fatigue failure prediction. The database took into account the influence of the fibre orientation, stress ratio and environmental conditions. The mentioned studies show that there is a

requirement of a fatigue failure method, which is able to predict the fatigue response independently of the influencing parameters (fibre orientation, load ratio, environmental conditions). However, none of the above-mentioned authors^{13,22} considered the influence of the wall thickness of the specimens on the fatigue performance of SFRPs.

In this investigation, an extensive database of fatigue data was created and evaluated, and the evolution of different mechanical properties, such as cyclic mean strain rate and energy-based quantities, were monitored. Based on these results, a modified different fatigue clustering parameter for fatigue curves of SFRPs was identified.

The paper is organized as follows – Section 2 describes the material, specimens and testing conditions, as well as the experimental procedures used in this study. In addition, the cyclic mechanical characteristics (cyclic mean strain rate, cyclic creep energy density and alternating energy density) observed during the tests are mentioned. Section 3 illustrates the evolution of these parameters during the fatigue testing and provides a summary of the fatigue endurance determined for the tested material. Furthermore, quasi-static tests were conducted and the microstructure of 1.6 mm and 3 mm plates was compared and discussed. In Section 4, fatigue failure parameters from the literature are presented together with a new alternating energy based fatigue parameter. Finally, the performance of the different fatigue failure parameters is discussed.

Nomenclature

ε	Strain	N_f	Cycles to failure
ε_{mean}	Mean strain	$N_{45\%}$	Cycles to failure at 45% lifetime
$\Delta\varepsilon$	Delta strain	$N_{55\%}$	Cycles to failure at 55% lifetime
ε_{max}	Maximum strain	$N_{f,calc.}$	Calculated number of cycles to failure
ε_{min}	Minimum strain	$N_{f,exp.}$	Experimental number of cycles to failure
σ_{mean}	Mean stress	$\dot{\varepsilon}_{mean}$	Cyclic mean strain rate
$\Delta\sigma$	Delta stress	W_{cr}	Cyclic creep energy density
σ_a	Alternating stress	AED	Alternating Energy Density
σ_{max}	Maximum stress	R_σ	Load ratio
σ_{min}	Minimum stress	T	Temperature
CT	Computer Tomography	RH	Relative Humidity
σ	Stress	t	Thickness
E	Young's Modulus	q. s.	Quasi static
$E_{Effective}$	Effective Young's Modulus	ABD	Anti Buckling Device
HCF	High Cycle Fatigue	k	Alternating parameter
FO	Fibre Orientation	UTS	Ultimate Tensile Strength
$wt.$	Weight	$SFRP$	Short Fibre Reinforced Polymer

2 Material and methods

2.1 Material and specimens manufacturing

The material under investigation is a PA6T/6I, filled with 50% weight short glass fibres, supplied under the trade name of Ultramid® Advanced T1000HG10 by BASF SE²³. To investigate the influence of the thickness in combination with the fibres orientation on the mechanical properties, dog bone specimens were extracted from injection moulded plates with two different thicknesses t (1.6 mm and 3 mm). One specimen per plate was machined out by milling at 0° and 90° with respect to the main flow direction as shown in Fig. 1(a). The shape of the specimens was designed with large radii to avoid failure in proximity of the grips. Fig. 1(b) showcases the specimen's shape and dimensions.

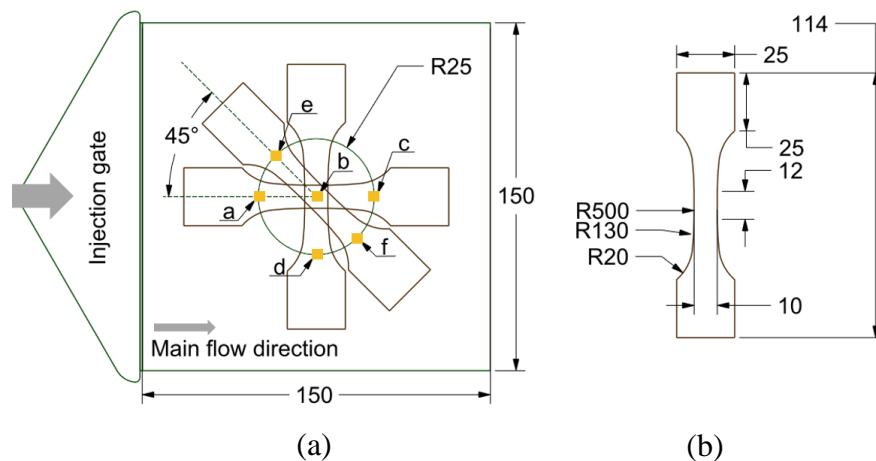


Figure 1: (a) Moulded plate dimension, dog bone cutting position and cutting sample position for fibre orientation analysis. (b) Specimen shape and dimensions. Dimensions are in (mm).

2.2 Experimental methods

2.2.1 μ CT measurements

Micro Computed Tomography (μ CT) scans were performed on Phoenix V|tome|x M300 computer tomography from Waygate Technologies²⁴ to measure the fibre orientation in the specimens. The tube voltage and current were 150 kV and 50 nA. A 0.5 mm aluminium filter directly before the x-ray tube was used. The samples were projected on a Dynamic 41|200p+ detector of 2048 x 2048 pixels, having a 200 nm pixel pitch. The 3D image was reconstructed from 2300 projections with an exposure time of 100 ms for each projection. The voxel resolution of the resulting image is 8 μ m. The rendering,

visualization and determination of the fibre orientation were done in the software VG Studio Max. 3.2 from Volume Graphics²⁵. Fig. 2(a) shows the simultaneous scanning procedure of three dog bones extracted at various angles from an injection-moulded plate that had the same thickness. The measured area was divided in three sections to maximize the scan resolution (Fig. 2(b)).

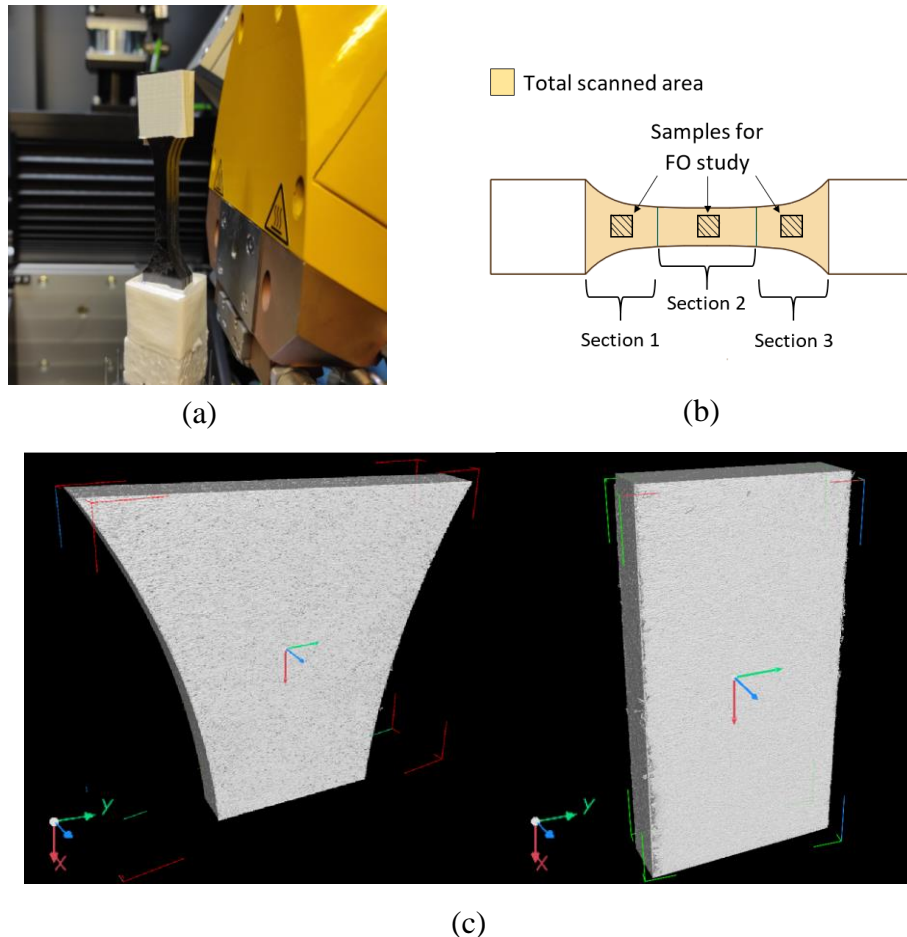


Figure 2: (a) Scanning procedure. (b) Specimen scanning area. (c) Three dimensional fibre orientation of the section 1 (left) and section 2 (right) for the specimen with 1.6 mm thickness.

2.2.2 *Quasi-Static and fatigue testing methods*

The testing campaign was performed at thyssenkrupp Presta AG. The test temperature was 80°C. The Relative Humidity (RH) was kept under 0.1% wt. and the specimens were sealed in individual bags after being manufactured, to prevent any change in RH prior to the experiment.

The quasi-static (q.s.) tests were conducted with an Inspect 300-1 Hegewald and Peschke test rig. To measure the deformation of the specimens during the q.s. experiments, a 3D optical measurement system GOM ARAMIS was used. For this purpose, a random speckle pattern was applied on the specimens. Since the specimens had a gloss black finish, they were first painted with matt black. Once the paint was dry, white speckle pattern were sprayed on them. The displacement rate was 1 mm/min. Five specimens per orientations and thickness were tested. To carry out tests at 80°C, a temperature chamber equipped with a digital temperature controller was used.

For the fatigue characterization, an Instron 8802 uniaxial servo hydraulic fatigue testing machine with an environmental chamber was used. A sinusoidal load function with constant amplitude at a frequency of 4 Hz was chosen. To track the evolution of strain, a contact extensometer (Instron, model 2620-603) with a gauge length of 10 mm was utilized. During testing, a Fluke thermal camera was used to track the specimen's surface temperature. This made it possible to guarantee that the surface temperature did not exceed the chosen test temperature by more than 5 °C. Complete specimen separation was the failure criterion. If a specimen did not break after 1E+6 cycles, it was considered a runout. Runouts were excluded for the computation of the parameters of the SN curve equation. Tension – tension and tension – compression tests were conducted while maintaining a constant load ratio $R_\sigma (= \sigma_{min} / \sigma_{max}) = 0.1, 0.5$ and -0.5 respectively. To prevent buckling during the compression phase of the tension-compression testing, a steel Anti-Buckling Device (ABD) was used. Fig. 3 shows how the ABD was installed. The ABD was not fixed within the machine clamps. Teflon sheets were installed between the specimen and the device to avoid friction effects.

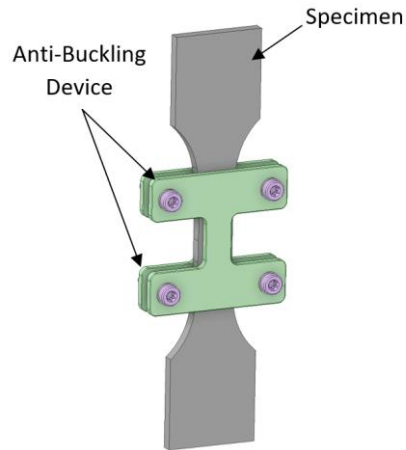


Figure 3: Anti-Buckling Device and application on a dog bone a specimen

2.2.3 Mechanical quantities

Several mechanical parameters were calculated and monitored during the fatigue tests. These were evaluated from the measured strain and the nominal stress.

Cyclic mean strain and cyclic mean strain rate. According to references ^{13,22,26}, first the minimum and maximum strain values for each cycle were measured. Fig. 4 depicts the trend of the minimum and maximum strain during fatigue testing. Based on these values, the cyclic mean strain evolution was determined according to Eq. (1).

$$\varepsilon_{mean} = \frac{\varepsilon_{max} + \varepsilon_{min}}{2} \quad (1)$$

The slope of the evolution of the cyclic mean strain defining the cyclic mean strain rate. Finally, the fatigue parameter is calculated by averaging the cyclic mean strain between 45% and 55% of the lifetime (Fig. 4).

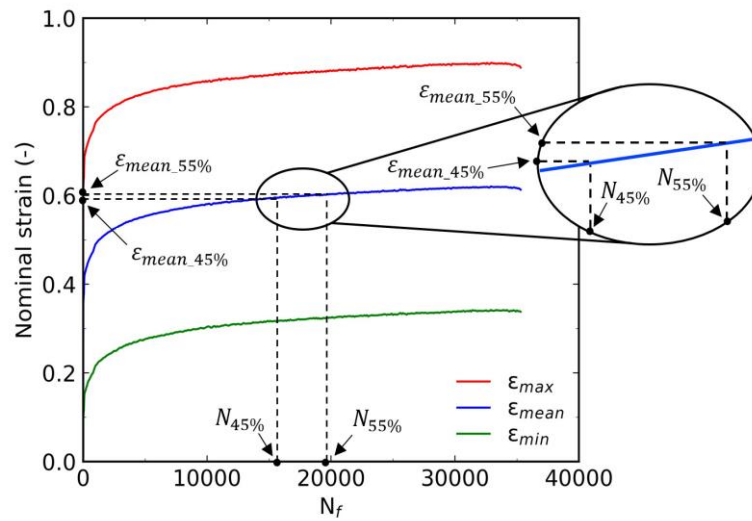


Figure 4: Axial strain evolution during a fatigue characterization

Each test is assessed according to the following fatigue parameter, which is determined as follows:

$$\dot{\epsilon}_{mean} = \frac{\epsilon_{mean_{55\%}} - \epsilon_{mean_{45\%}}}{N_{55\%} - N_{45\%}} \text{frequency} \quad (2)$$

To investigate the effect of alternative intervals, we conducted a parametric study examining cyclic mean strains between 47% and 53% of the lifetime, as well as between 42% and 58% of the lifetime.

Cyclic creep energy density. The influence of the mean stress on fatigue behaviour has been studied earlier⁷⁻¹⁰. A parameter, called cyclic creep energy density, calculated by multiplying the cyclic mean strain rate $\dot{\epsilon}_{mean}$ with the mean stress σ_{mean} (see Eq. (3)) was suggested by Santharam et al.¹³. It combines the cyclic energy to a parameter related to cyclic creep. The authors used the cyclic creep energy density parameter for the lifetime estimation for short fibre reinforced polymers.

$$W_{cr} = \sigma_{mean} \dot{\epsilon}_{mean} \quad (3)$$

AED - Alternating Energy Density. High cycle fatigue is usually caused by alternating loads in the elastic range. Due to the influence in high cycle fatigue of the alternating stresses, a modified expression of Eq. (3) is proposed, named alternating energy density, which combines the cyclic mean strain rate parameter to the alternating

stress. The proposed fatigue parameter, depending on the alternating stress, is expressed as follow:

$$AED = \dot{\epsilon}_{mean} \sigma_a \quad (4)$$

Considering the Eq. (3), the cyclic creep energy density can also be expressed as follows:

$$W_{cr} = \frac{(1 + R_\sigma)}{(1 - R_\sigma)} \sigma_a \dot{\epsilon}_{mean} = \frac{(1 + R_\sigma)}{(1 - R_\sigma)} AED \quad (5)$$

The parameters AED and W_{cr} are interchangeable by using Eq. 6:

$$AED = W_{cr} k \quad (6)$$

where it is easy to demonstrate that the parameter k is calculated according to Eq. (7).

$$k = \frac{1}{\frac{(1 + R_\sigma)}{(1 - R_\sigma)}} \quad (7)$$

Fig. 5 shows how the parameter k varies as a function of the load ratio, R_σ . As shown, the value of k is smaller or greater than 1 if the load ratio is positive or negative, respectively.

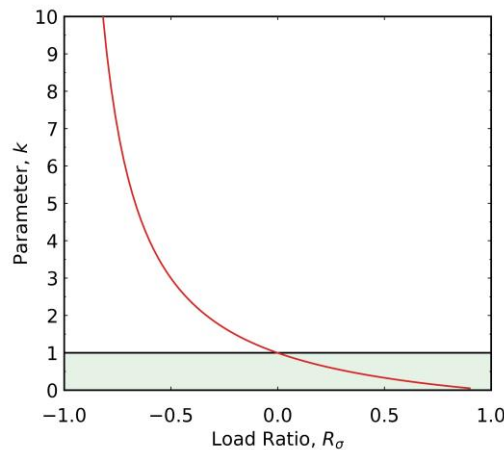


Figure 5: The parameter k as a function of the load ratio R_σ

3 Experimental results

3.1 Microstructure – Fibre orientation analysis

In Fig. 6(a) and 6(b), for the scanned position b (centre of the plate), the measured orientation tensor components a_{xx} , a_{yy} and a_{zz} ²⁷ are plotted against the position through the specimen's thickness. The coordinate system considered is reported in Fig. 1(a), i.e. the x-axis is along the flow direction and z-axis points in thickness direction of the plate. For the scanned positions b the off-diagonal components of the matrix ranged between 0.07 and -0.03 for the 1.6 mm specimen and between 0.03 and -0.04 for the 3 mm specimen and were thus considered negligible.

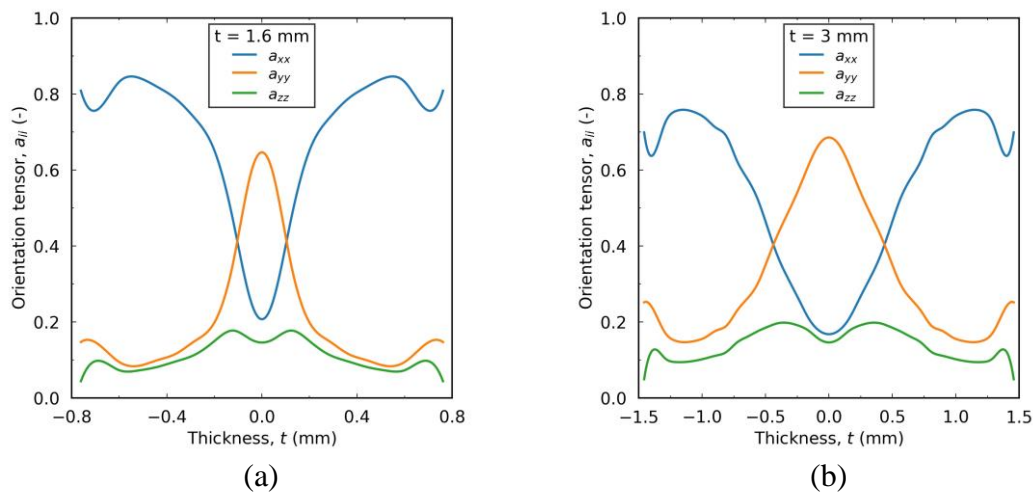


Figure 6: Orientation tensor distribution for (a) 1.6 mm and (b) 3 mm plate thickness

According to Fig. 6, the width of the non-oriented zone grows as the thickness increases and the fibres' alignment with respect to the flow direction becomes less prominent. Proportionally to the thickness of the entire specimen, the thickness of the core layer grows from around 1/8 at $t = 1.6$ mm to 1/4 at $t = 3$ mm. In the skin layer, contrary to the shell layer where fibres are mainly aligned in flow direction, many fibres exhibit a transverse orientation (y-axis). Similar results were reported by De Monte et al.⁴

In Fig. 7(a) and Fig. 7(b), the orientation tensor component a_{xx} as a function of the thickness for the 1.6 mm and 3 mm sample thickness is plotted respectively.

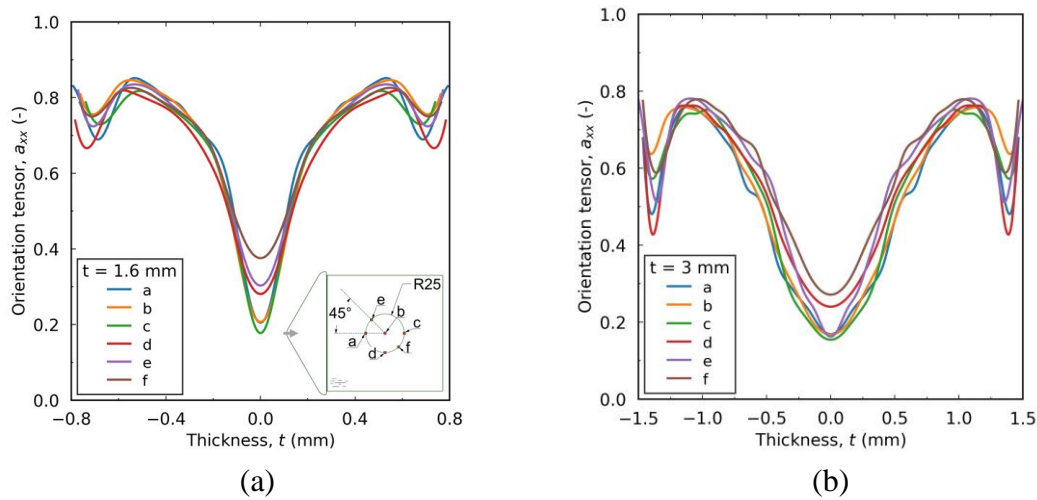


Figure 7: Fibre orientation tensor component in injection moulding direction a_{xx} for two specimen thicknesses (a) 1.6 mm and (b) 3 mm. Six scanned locations according to Fig. 1(a).

The mean through the thickness fibre orientation tensor components a_{xx} , a_{yy} and a_{zz} for the scanned samples are presented in Table 1(a), 1(b) and 1(c). For the two thicknesses considered, the a_{xx} displays a consistent distribution of the computed mean values at the scanned positions a , b , and c . Stadler et al.²⁸ made a similar consideration when the FO along the flow direction was nearly constant. For the thicknesses 1.6 mm and 3 mm, the range of the mean value for the orientation tensor component a_{xx} , considering all the extracted samples, was equal to 0.05 and 0.06 respectively. Comparing a_{xx} , a difference of 7.5% and 13% between scanned position c and f was detected for the 1.6 mm and for the 3 mm thickness respectively.

Moreover, it is interesting to note that the scanned positions d , e and f show a lower fibre alignment in the core only. An analysis of the off-diagonal matrix components for the above mentioned scanned positions shows that the a_{xy} ranged between 0.22 and -0.03 for the 1.6 mm specimen and between 0.02 and -0.19 for the 3 mm specimen. In Fig. 8 the orientation component a_{xy} for the six scanned positions is plotted.

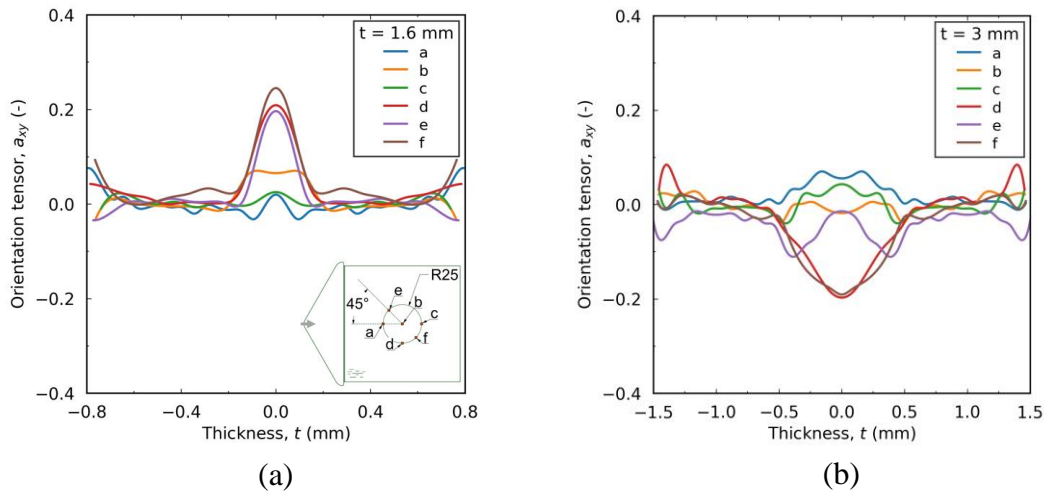


Figure 8: Fibre orientation tensor components a_{xy} for two specimen thicknesses (a) 1.6 mm and (b) 3 mm. Six scanned locations according to Fig. 1(a).

Table 1: Evaluation of the average a_{xx} , a_{yy} and a_{zz} distribution for six samples, scanned at six different positions according to Fig. 1(a) for two plate thicknesses

Scanned position	Average a_{xx}		Average a_{yy}		Average a_{zz}	
	3 mm	1.6 mm	3 mm	1.6 mm	3 mm	1.6 mm
<i>a</i>	0.54	0.69	0.31	0.20	0.15	0.11
<i>b</i>	0.55	0.7	0.31	0.20	0.14	0.1
<i>c</i>	0.54	0.66	0.31	0.22	0.15	0.12
<i>d</i>	0.60	0.68	0.25	0.20	0.15	0.12
<i>e</i>	0.58	0.71	0.29	0.19	0.13	0.10
<i>f</i>	0.61	0.71	0.26	0.18	0.13	0.11
Δ	0.06	0.05	0.07	0.04	0.02	0.02

3.2 Quasi-Static and fatigue material characterization

Fig. 9 compares the engineering stress vs. the engineering strain behaviour between the analysed fibre orientation for the two thicknesses. The strains at failure vary between 1.5% and 2.4%, depending on the FO angle. To protect the confidentiality of the experimental results, a normalization approach for calculating stress values were used. All stresses shown in the q.s. and fatigue data are dividing by the same constant factor. This approach allowed us to report the results in a meaningful way while safeguarding the confidentiality of the experimental data.

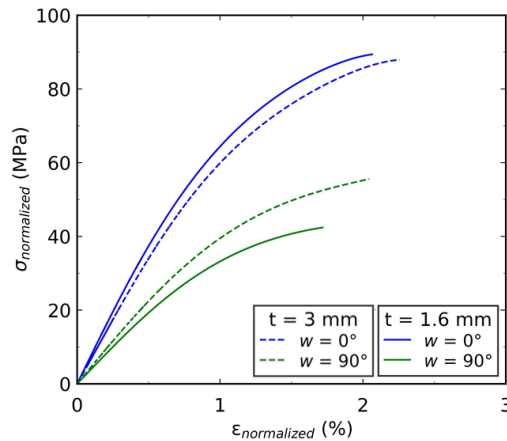


Figure 9: Comparison of the q.s. behaviour for two different orientations and two thicknesses $t = 1.6$ mm and $t = 3$ mm.

Each curve has an initially linear strain response, which is thereafter followed by a nonlinear response until failure.

The $t = 1.6$ mm specimen displays a substantial level of anisotropy. According to samples with $t = 3$ mm, this anisotropy becomes less noticeable as the specimen thickness increases. The varied FO distribution is considered responsible for the anisotropy's decrease with thickness. μ CT-measurements show that the plate with 1.6 mm thickness has well aligned fibres in main flow direction and a small relative thickness of the core, while the 3 mm plate has less aligned fibres and a larger core layer. A similar observation was reported by De Monte et al. ⁴ and Friedrich ².

Fig. 10 shows the fatigue results in nominal stress amplitudes against the number of cycles to failure N_f . The number of cycles to failure N_f is interpolated using Basquin law:

$$\sigma_a = aN_f^b \quad (8)$$

where a and b are fitting parameters.

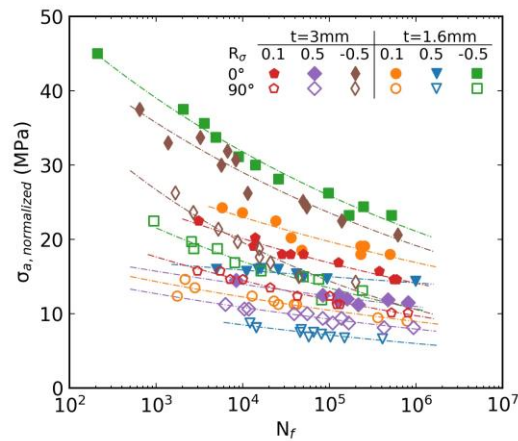
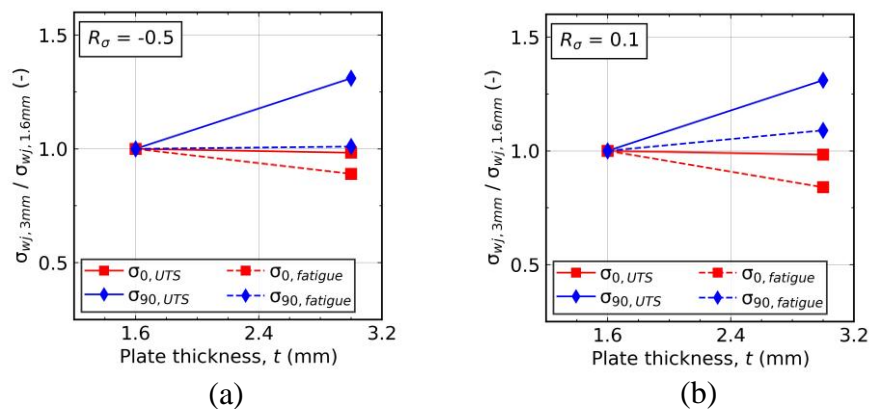
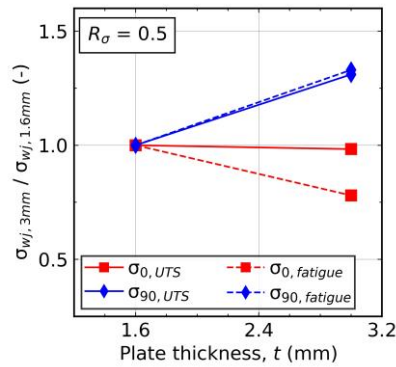


Figure 10: Normalized SN curves for three load ratios, two specimen thicknesses and two orientations (dashed lines correspond to power-law fits, using Eq. (7)).

Fig. 11 shows the normalized UTS and the normalized fatigue strength (residual strength at $N_f = 10E+6$) as a function of specimen thickness with respect to the load ratios. The plotted UTS and fatigue strength for the specimen extracted at $w = 0^\circ$ and $w = 90^\circ$ were normalized by the UTS and fatigue strength of the $t = 1.6$ mm specimen. The influence of the thickness on fatigue strength is more significant when compared to its influence on q.s. strength. In Fig. 11(a), the results for $R_\sigma = -0.5$ are plotted. The failure strength remains constant (increase of 1%) for the specimen milled at $w = 90^\circ$. A decrease in failure strength of 11% was measured for the specimens extracted in main flow direction. For the experimental tests performed with a load ratio of $R_\sigma = 0.1$ (Fig. 11(b)), the fatigue strength increases up to 9% for the specimen extracted at $w = 90^\circ$. On the other hand, a decrease in fatigue strength of 16% was detected for the specimen milled at $w = 0^\circ$. Fig. 11(c) shows an increase in fatigue strength of 33% for specimen milled at $w = 90^\circ$. For the longitudinal extracted specimens, a 22% decrease in fatigue strength was detected.





(c)

Figure 11: Influence of thickness on normalized fatigue strength parameters for (a) $R_\sigma = -0.5$, (b) $R_\sigma = 0.1$ and (c) $R_\sigma = 0.5$ compared to corresponding trends under quasi static loading

Fig. 9 have shown that the quasi-static (UTS) properties of the material depend on specimen thickness. In particular, while the $t = 3$ mm specimen exhibited only slight anisotropy, the $t = 1.6$ mm specimen demonstrated significant anisotropy. This finding is consistent with the observed microstructural changes in thicker specimens, which have a higher relative core layer and reduced fibre alignment in the main flow direction, as confirmed by μ CT analysis. The influence of the thickness on the fatigue strength differs significantly from the conclusions reported for the quasi static results. Furthermore, it appears that the effect of thickness may also vary depending on the specific loading conditions, with different trends observed for tension-compression (Fig. 11(a)) and tension-tension (Fig. 11(c)) loading. The findings suggest that failure mechanisms vary depending on whether the material is subjected to quasi-static or cyclic loading. These observations agree with the findings reported by other authors^{6,29}. As reported by Horst and Spoomaker³⁰, during q.s. loading the damage occur in the matrix, in the fibres and at the fibre-matrix interface, while fatigue-loading causes damage mainly in the fibre-matrix interface.

4 Discussion on the fatigue parameters

4.1 Fatigue parameters and performance

Fig. 12 show the (a) cyclic mean strain rate, (b) the cyclic creep energy density and the (c) alternating energy density parameters calculated for the different specimens, respectively.

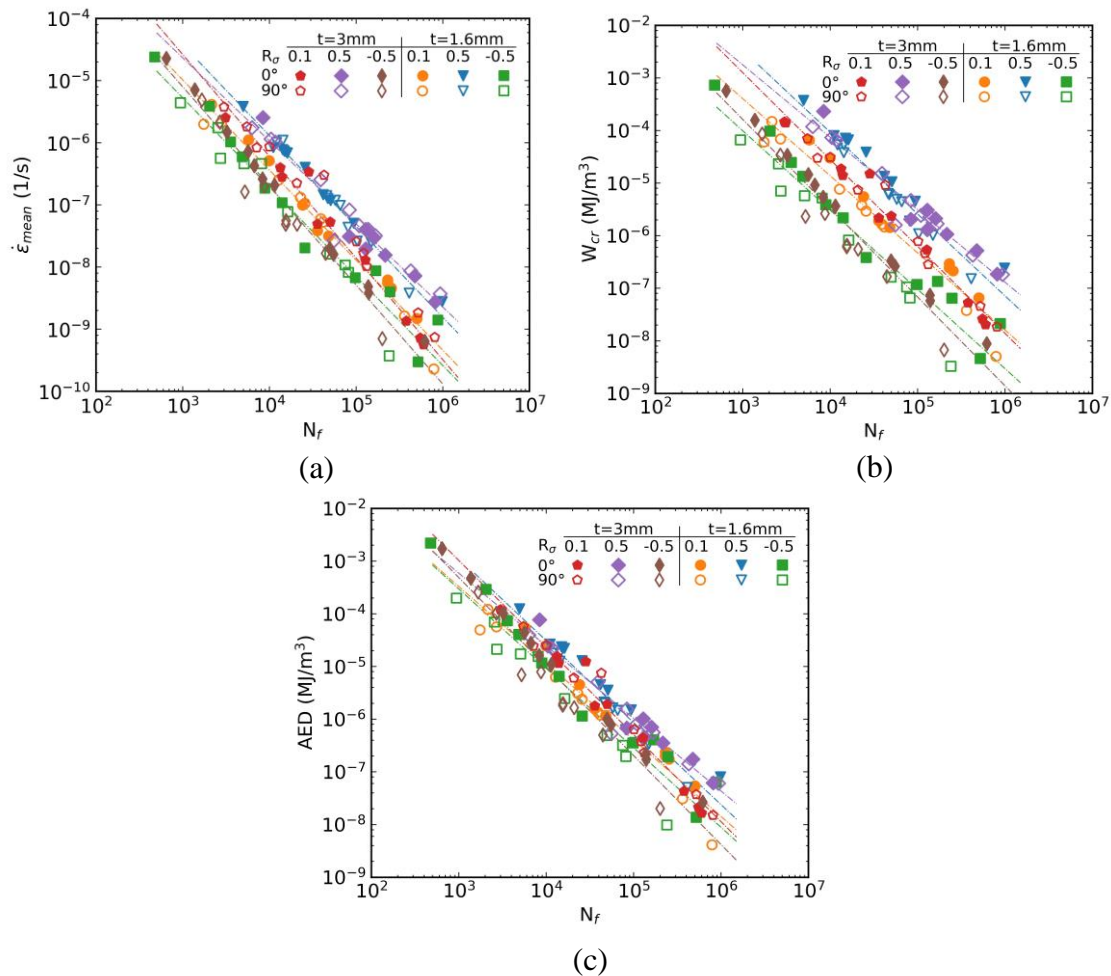


Figure 12: (a) Cyclic mean strain rate, (b) cyclic creep energy density and (c) alternating energy density calculated at mid-life vs. cycles to failure for the investigated load ratios, two orientations and two thicknesses (dashed lines correspond to power-law fits, using one set of parameters for each thickness and load ratio).

A thickness independency for the three analysed fatigue parameters could be visually detected. Additionally, it is visible that the cyclic mean strain rate and the cyclic creep energy density fatigue parameters were able to cluster the data independently from the orientations, while they were dependent on the applied load ratio. This is coherent with the findings of ^{13,22}. The alternating energy density fatigue parameter managed to group visibly almost all data regardless of the orientations, thicknesses and load ratios.

To assess the parameter performance of clustering the data, a quantitative analysis was performed.

The following power law is used to express the relationship between the number of cycles to failure and the considered fatigue parameter:

$$\text{Fatigue parameter} = AN_f^q \quad (9)$$

The Eq. (9) can be reformulated for the evaluation of the calculated lifetime as follows:

$$N_{f,calculate} = C(\text{Fatigue parameter})^p \quad (10)$$

with:

$$C = A^{-\frac{1}{q}} \quad \text{and} \quad p = \frac{1}{q} \quad (11)$$

The coefficients, A and q are material dependent. The coefficient set identification was carried out on the 3 mm specimen, extracted longitudinal to main flow direction and tested with a load ratio of $R_\sigma = 0.1$. The used coefficients are reported in Table 2.

Table 2: Material dependent coefficients for the accuracy calculation of the considered fatigue parameters

$t = 3 \text{ mm}$ $w = 0^\circ$ $R_\sigma = 0.1$	Coefficients for accuracy analysis		
	$\dot{\epsilon}_{mean}$	W_{cr}	AED
A	2.15	215.52	176.32
q	-1.637	-1.714	-1.714

To determine and compare the fatigue parameter performance, the $N_{f,calculated}$ and $N_{f,experimental}$ are compared. The estimated lifetime $N_{f,calculated}$ is calculated according to Eq. (10). Scatter bands of factor two and three are marked in dashed and dotted lines respectively.

Fig. 13 compares the number of cycles to failure calculated using the cyclic mean strain rate (a), the cyclic creep energy density (b) and the alternating energy density (c) material coefficients to the experimental number of cycles.

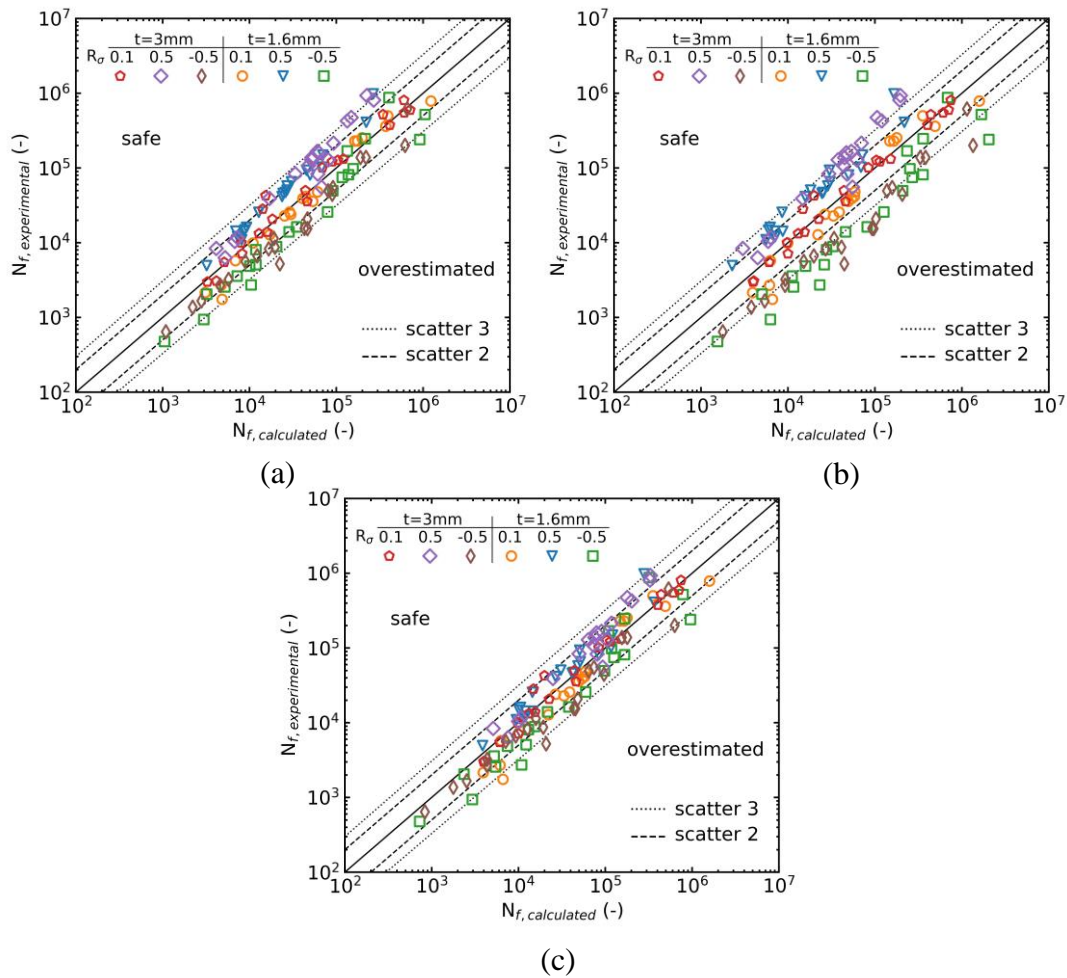


Figure 13: Calculated fatigue lifetime using Eq. (10) vs. experimental number of cycle to failure based on a single set of material coefficients for (a) $\dot{\epsilon}_{mean}$, (b) W_{cr} and (c) AED calculated on the specimen ($t = 3 \text{ mm}$) extracted longitudinal to main flow direction and tested with a load ratio of $R_\sigma = 0.1$.

Cyclic mean strain rate. By only using a single set of parameters, 69% of the calculated lifetime lays within scatter band two, whereas 93% are within scatter band three. For the tests performed at $R_\sigma = 0.5$, an underestimation can be detected. However, in the case of the negative load ratio the $\dot{\epsilon}_{mean}$ based fatigue parameter tends to overestimate the cycles to failure. A further investigation was performed to evaluate the dependency of the used interval for the fatigue parameter calculation. Figure 14 illustrates the cyclic mean strain rates evaluated within two additional distinct intervals: (a) 42% to 58% and (b) 47% to 53% of the lifetime. The results are graphically represented as a function of the cycles to failure. Detailed accuracy findings are reported in Table 3. As

shown, the 45% to 55% interval proved the highest accuracy; this is also the interval most widely used in the literature^{13,22,26}. Taking these results into account, this interval was consistently applied throughout the study.

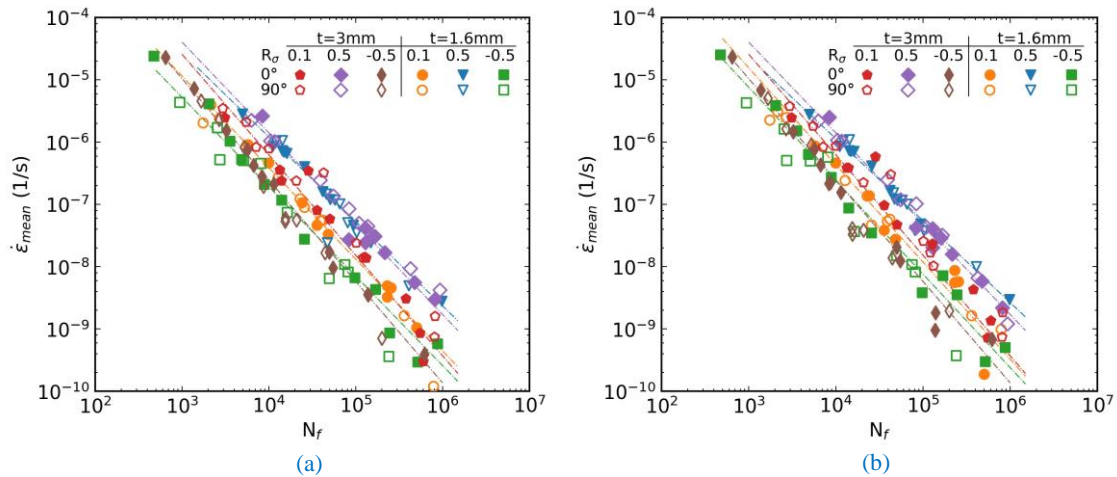


Figure 14: Cyclic mean strain rate evaluated between (a) 42% to 58 and (b) 47% to 53% vs. cycles to failure for the investigated load ratios, two orientations and two thicknesses (dashed lines correspond to power-law fits, using one set of parameters for each load ratio).

Table 3: Accuracy results for the cyclic mean strain rate evaluated between 42% - 58%, 45% - 55% and 47% - 53% for scatter band two and scatter band of three

$t = 3 \text{ mm}$ $w = 0^\circ$ $R_\sigma = 0.1$	Accuracy results for different ranges		
	$\dot{\epsilon}_{mean}$ (42% - 58%)	$\dot{\epsilon}_{mean}$ (45% - 55%)	$\dot{\epsilon}_{mean}$ (47% - 53%)
Scatter 2	63%	69%	69%
Scatter 3	93%	93%	89%

Cyclic creep energy density. The accuracy analysis for the fatigue parameter based on the cyclic creep energy density yields results that are comparable to those of the cyclic mean strain rate fatigue parameter. As shown in Fig. 13(b), 47% of the calculated lifetime lays within scatter band two, whereas 68% are within scatter band three. However, there is a significant average discrepancy between the predicted and empirically determined cycles to failure. In comparison to the cyclic mean strain rate fatigue parameter, the tendency to overstate the negative load ratio is higher.

AED - Alternating Energy Density. In Fig. 13(c) the performance analysis results are presented. The quantitative performance analysis shows that 81% of the calculated lifetime lays within scatter band two, whereas 95% are within scatter band three.

4.2 Comparison of performance

The cyclic mean strain rate ($\dot{\epsilon}_{mean}$), the cyclic creep energy density (W_{cr}) and the alternating energy density (AED) based criteria are used to predict fatigue failure.

The newly proposed AED parameter showed higher prediction capabilities than the other tested parameters. This is explained in the following.

First of all, it must be noticed that R_σ is directly proportional to the mean stress σ_{mean} but inversely proportional to the alternating stress σ_a : for increasing R_σ , σ_{mean} increases and σ_a decreases. The opposite occurs for decreasing R_σ . Moreover, $\dot{\epsilon}_{mean}$ is a parameter that is mainly affected by the mean stress σ_{mean} . Indeed, curves relative to higher R_σ ratios, where σ_{mean} is generally higher, show higher values of the $\dot{\epsilon}_{mean}$ parameter (see Figure 12a).

The cyclic creep energy density (W_{cr}) multiplies $\dot{\epsilon}_{mean}$ by σ_{mean} , thus increasing the differences between the curves and considering the effects of the mean stress twice (both via $\dot{\epsilon}_{mean}$ and σ_{mean}) while neglecting the effects of the alternating stress σ_a . Indeed, the W_{cr} is less accurate than $\dot{\epsilon}_{mean}$.

Conversely, the AED parameters multiplies $\dot{\epsilon}_{mean}$ by σ_a , which is higher for lower values of R_σ and vice versa. Therefore, the curves tend to cluster rather than separate. In addition, both the effect of the mean stress (via $\dot{\epsilon}_{mean}$) and the alternating stress σ_a are considered in the AED parameter.

In conclusion, the AED parameter is more accurate than W_{cr} because it is able to take into account both the effects of the mean and alternating stress on the fatigue life of the material.

To further check the accuracy of the AED parameter, results published in ¹³ were used. The database was generated for dog bone specimens extracted from three different orientations ($w = 0^\circ, 45^\circ$ and 90°) to the injection moulding direction and for two

environmental conditions. For the environmental conditions RH50% and $T = 80^{\circ}\text{C}$, the load ratios used were $R_{\sigma} = -0.5, -0.2, 0.1, 0.3, 0.5$ and 0.7 . For tests performed at $T = 23^{\circ}\text{C}$ and RH80% the load ratios used were $R_{\sigma} = -0.5, -0.2$ and 0.1 . In Fig. 15(a) the cyclic creep energy density results are plotted against the cycles to failure N_f . The solid lines represent the power law for one load ratio, three orientations and two environmental conditions. Even if the results were normalized, the previously presented parameter k allows us to calculate the AED independent of the real mechanical properties such as σ_a . Fig. 15(b) shows the AED parameter calculated according to Eq. (6) and Eq. (7).

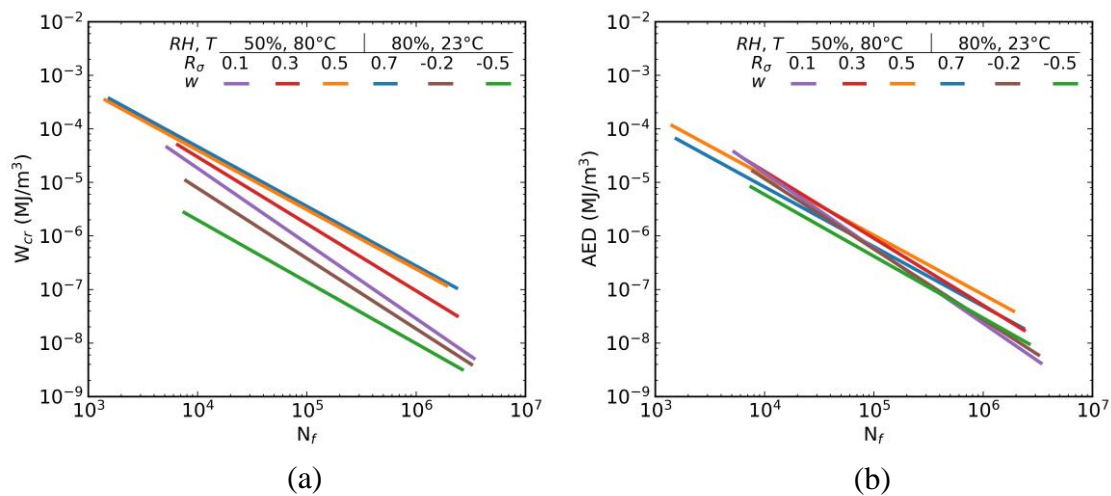


Figure 15: (a) Cyclic creep energy density and (b) AED - Alternating Energy Density at for the data presented in ¹³ (solid lines correspond to power-law fits, using one set of parameters for each load ratio).

Data in Fig 15(b) are clearly more clustered. From a qualitative point of view, the fatigue parameter was able to group the data independently from parameters such as thickness, load ratio, environmental conditions, and orientation. To be able to perform an accuracy analysis on the results of ¹³, the experimental results would be needed.

Based on our tests, in terms of a quantitative fatigue prediction accuracy, the alternating energy density fatigue parameter shows good results. Additionally, the application of the AED requires a minimum experimental effort.

At present, AED lacks the capability to predict SN curves. To achieve this, a constitutive model describing the cyclic behaviour (see for example Launay et al. ³¹) is required to

evaluate the mean strain rate. Future research should prioritize the development of such a method. The input parameters for this model would include the mean strain rate, stress amplitude, and the C and p parameters (whose identification requires only one SN curve, as demonstrated in this paper). The desired output would be the number of cycles to failure.

5 Conclusions

In this work, the fatigue behaviour of a PA6T/6I-GF50 material was investigated using specimens of two different thicknesses (1.6 mm and 3 mm) and two orientations (0° and 90°) milled from injection moulded plates. Fatigue testing was conducted under three different load ratios (-0.5, 0.1, and 0.5), monitoring the maximum and minimum strain during characterization. A microstructural evaluation of the injection moulded plate and as a function of the thickness was also performed using μ CT scans. Based on the presented results, the following conclusions can be drawn:

- The three fatigue failure parameters considered, namely the cyclic mean strain rate, cyclic creep energy density, and the newly proposed AED (Alternating Energy Density), successfully clustered the data independently of specimen thickness.
- Load ratio dependency was observed for the cyclic mean strain rate and cyclic creep energy density fatigue failure parameters.
- The AED parameter effectively grouped 95% of the data within the scatter band three. The parameter thus proved to be independent of the main fibre orientation, specimens' thickness, and load ratio.
- An accuracy comparison proved the newly proposed AED parameter to be more accurate than the other considered parameters. This was likely due to the fact that the AED is able to consider both the effect of the mean and alternating stress or strain components.

Further investigations should focus on applying the fatigue parameter to notched specimens, multiaxial stress states, or components to determine its applicability to complex topologies. Additionally, exploring the implementation of AED in numerical methodologies using existing Finite Element tools could be a promising approach.

Acknowledgements

The authors gratefully acknowledge thyssenkrupp Presta AG and BASF SE for supporting this work. The authors wish to thank Dr. Andreas Radtke (BASF SE) for the help in moulding the plates and supporting this work and Thorsten Wiege (thyssenkrupp Presta AG) for the help during the material testing. The authors gratefully acknowledge Prof. Dr. Gianpiero Mastinu (Politecnico di Milano) for the useful discussions and proofreading. Finally, FEF gratefully acknowledges to Sabina Hodzic (thyssenkrupp Presta AG) for her proofreading.

References

1. Bernasconi A, Davoli P, Basile A, Filippi A. Effect of fibre orientation on the fatigue behaviour of a short glass fibre reinforced polyamide-6. *Int J Fatigue*. 2007;29(2):199-208.
2. Friedrich K. Microstructural efficiency and fracture toughness of short fiber/thermoplastic matrix composites. *Compos Sci Technol*. 1985;22(1):43-74.
3. Horst JJ. *Influence of fibre orientation on fatigue of short glassfibre reinforced Polyamide* [Doctoral thesis]: Industrial Design Engineering, Delft University; 1997.
4. Monte MD, Moosbrugger E, Quaresimin M. Influence of temperature and thickness on the off-axis behaviour of short glass fibre reinforced polyamide 6.6 – Quasi-static loading. *Compos Part Appl Sci Manuf*. 2010;41(7):859-871.
5. Bernasconi A, Cosmi F, Dreossi D. Local anisotropy analysis of injection moulded fibre reinforced polymer composites. *Compos Sci Technol*. 2008;68(12):2574-2581.
6. Monte MD, Moosbrugger E, Quaresimin M. Influence of temperature and thickness on the off-axis behaviour of short glass fibre reinforced polyamide 6.6 – cyclic loading. *Compos Part Appl Sci Manuf*. 2010;41(10):1368-1379.
7. Mallick PK, Zhou Y. Effect of mean stress on the stress-controlled fatigue of a short E-glass fiber reinforced polyamide-6,6. *Int J Fatigue*. 2004;26(9):941-946.
8. Mortazavian S, Fatemi A. Effects of mean stress and stress concentration on fatigue behavior of short fiber reinforced polymer composites. *Fatigue Fract Eng M*. 2016;39(2):149-166.
9. Sauer JA, McMaster AD, Morrow DR. Fatigue behavior of polystyrene and effect of mean stress. *J Macromol Sci Part B*. 2008;12(4):535-562.

10. Sonsino CM, Moosbrugger E. Fatigue design of highly loaded short-glass-fibre reinforced polyamide parts in engine compartments. *Int J Fatigue*. 2008;30(7):1279-1288.
11. Bernasconi A, Kulin RM. Effect of frequency upon fatigue strength of a short glass fiber reinforced polyamide 6: A superposition method based on cyclic creep parameters. *Polym Composite*. 2009;30(2):154-161.
12. Eftekhari M, Fatemi A. On the strengthening effect of increasing cycling frequency on fatigue behavior of some polymers and their composites: Experiments and modeling. *Int J Fatigue*. 2016;87:153-166.
13. Santharam P, Marco Y, Saux VL, Saux ML, Robert G, et al. Fatigue criteria for short fiber-reinforced thermoplastic validated over various fiber orientations, load ratios and environmental conditions. *Int J Fatigue*. 2020;135:105574.
14. Benoit A, Maitournam MH, Rémy L, Oger F. Cyclic behaviour of structures under thermomechanical loadings: application to exhaust manifolds. *Int J Fatigue*. 2012;38:65-74.
15. Constantinescu A, Dang Van K, Maitournam M. A unified approach for high and low cycle fatigue based on shakedown concepts. *Fatigue Fract Eng M*. 2003;26(6):561-568.
16. Klimkeit B, Castagnet S, Nadot Y, Habib AE, Benoit G, et al. Fatigue damage mechanisms in short fiber reinforced PBT+PET GF30. *Mater Sci Eng*. 2011;528(3):1577-1588.
17. Kujawski D, Ellyin F. A unified approach to mean stress effect on fatigue threshold conditions. *Int J Fatigue*. 1995;17(2):101-106.
18. Amiable S, Chapuliot S, Constantinescu A, Fissolo A. A comparison of lifetime prediction methods for a thermal fatigue experiment. *Int J Fatigue*. 2006;28(7):692-706.
19. Jegou L, Marco Y, Le Saux V, Calloch S. Fast prediction of the Wöhler curve from heat build-up measurements on Short Fiber Reinforced Plastic. *Int J Fatigue*. 2013;47:259-267.
20. Launay A, Maitournam M, Marco Y, Raoult I. Multiaxial fatigue models for short glass fibre reinforced polyamide. Part II: Fatigue life estimation. *Int J Fatigue*. 2013;47:390-406.
21. Meneghetti G, Quaresimin M. Fatigue strength assessment of a short fiber composite based on the specific heat dissipation. *Compos Part B Eng*. 2011;42(2):217-225.
22. Raphael I, Saintier N, Rolland H, Robert G, Laiarinandrasana L. A mixed strain rate and energy based fatigue criterion for short fiber reinforced thermoplastics. *Int J Fatigue*. 2019;127:131-143.

23. BASF SE, Ultramid® Advanced T1000 (PA, PPA). https://plastics-rubber.basf.com/global/en/performance_polymers/products/ultramid_advanced_t1000.html.
24. Waygate Technologies, Phoenix Micro CT Scanner. <https://www.bakerhughes.com/waygate-technologies/industrial-radiography-and-ct/phenix-advanced-industrial-xray-and-ct/phenix-vtomex-m-high-speed-3d-ct-scanner>.
25. Volume Graphics, VGSTUDIO MAX. <https://www.volumegraphics.com/de/produkte/vgsm.html>.
26. Gillet S, Jacopin T, Joannès S, Bedrici N, Laiarinandrasana L. Short-term creep and low cycle fatigue unified criterion for a hybridised composite material. *Int J Fatigue*. 2022;155:106571.
27. Advani SG, Tucker III CL. The use of tensors to describe and predict fiber orientation in short fiber composites. *Journal of rheology*. 1987;31(8):751-784.
28. Stadler G, Primetzhofer A, Pinter G, Grün F. Evaluation and consideration of local specimen material properties in lifetime prediction of short fiber-reinforced PA6T/6I. *Fatigue Fract Eng M*. 2022;45(4):980-990.
29. Lang R, Manson J, Hertzberg R. Mechanisms of fatigue fracture in short glass fibre-reinforced polymers. *J Mater Sci*. 1987;22:4015-4030.
30. Horst J, Spoomaker J. Fatigue fracture mechanisms and fractography of short-glassfibre-reinforced polyamide 6. *J Mater Sci*. 1997;32:3641-3651.
31. Launay A, Maitournam M, Marco Y, Raoult I, Szymtka F. Cyclic behaviour of short glass fibre reinforced polyamide: Experimental study and constitutive equations. *Int J Plasticity*. 2011;27(8):1267-1293.